



## Porosity and fractal study of functionalized carbon nanofibers: Effects of the functionalization degree on hydrogen storage capacity

Félix Galindo-Hernández <sup>a</sup>, Benjamín Portales <sup>a</sup>, José M. Domínguez <sup>a,\*</sup>, Deyanira Angeles-Beltrán <sup>b</sup>

<sup>a</sup> Instituto Mexicano del Petróleo (IMP), Eje Central Lázaro Cárdenas Norte 152 Col. San Bartolo Atepehuacan, México D.F. C.P. 07730, Mexico

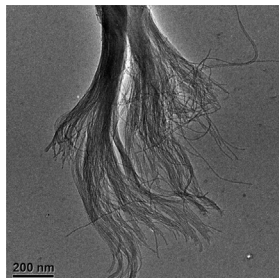
<sup>b</sup> Universidad Autónoma Metropolitana (UAM-A), Av. San Pablo 180, Col. Reynosa Tamaulipas, México D.F. C.P. 02200, Mexico



### HIGHLIGHTS

- Functionalized carbon nanofibers may be suitable for hydrogen storage.
- Hydrogen adsorption capacity depends on the functionalization degree.
- Changes on the surface are assessed by numerical calculations of fractal dimension.

### GRAPHICAL ABSTRACT



### ARTICLE INFO

#### Article history:

Received 16 April 2014

Received in revised form

19 June 2014

Accepted 23 June 2014

Available online 7 July 2014

#### Keywords:

Functionalized carbon nanofibers

Surface fractal dimension

High hydrogen storage capacity

NLDFT

### ABSTRACT

Carbon nanofibers are produced by siliceous SBA-15 type materials and the casting method. The nanofibers are functionalized by  $\text{HNO}_3$  attack in aqueous phase under microwave radiation.  $\text{N}_2$  sorption data are treated by Non-Local Density Functional Theory and Quenched Solid Density Functional Theory to determine advanced adsorption among other textural properties. The functionalization degree of carbon nanofibers and their hydrogen storage capacity are mainly investigated by FTIR spectroscopy, capacitance studies and analysis of the fractal dimension of the surface. This latter in two ways: i) using the Neimark–Kiselev equation with  $\text{N}_2$  sorption data and ii) using Box-counting, Information and Perimeter-area methods on TEM photomicrographs. The hydrogen storage testing reveals that functionalized carbon nanofibers adsorb hydrogen above 200% with respect to unfunctionalized carbon nanofibers. This effect is attributed to: i) the creation of extra spacing between contiguous nanofibers, as a consequence of mutual repulsion between the  $-\text{COOH}$  groups and ii) increase of volume intrawall.

© 2014 Elsevier B.V. All rights reserved.

## 1. Introduction

Hydrogen is an actual subject of research [1–4] because it is ideal for clean energy production and for potential sustainable applications. However, an effective and reliable hydrogen storage

system is still searched, which could override some actual limitations for the widespread use of hydrogen as a newer energy source. In this respect, the search of new materials for storing hydrogen safely continues still and among the most outstanding materials found are graphite and the metal decorated  $\text{TiO}_2$  nanoparticles [5], nitrogen-containing carbon spheres [6] and hybrid nickel/metal-hydride materials. [7]. A number of physical, chemical and electrochemical methods have been applied recently [8–10] to improve the knowledge about the mechanisms taking place at the molecular

\* Corresponding author. Tel.: +52 55 9175 8392.

E-mail addresses: [jmdoming@imp.mx](mailto:jmdoming@imp.mx), [jmdoming@msn.com](mailto:jmdoming@msn.com) (J.M. Domínguez).

level during hydrogen storage in some materials; however, there are still opportunities for developing more reliable materials, which might cover both safety and economical aspects [11]. In this respect, carbonaceous materials like hollow spheres, nanofibres and carbon nanotubes, have been synthesized and tested, due to their high surface area, low gas–solid interactions, high hydrogen uptake capacity and quick desorption properties [12–14]. In particular, several investigations on the hydrogen uptake capacity of carbon nanospheres [15] and nanofibres have been carried out, but their performance for hydrogen storage capacity in function of the surface functional groups has not been studied further. Thus, the present work focused on the effects of the functionalization on the carbon nanofibers (FCNFs<sup>1</sup>); for this, FCNFs materials were prepared by the casting method using sucrose solutions embedded into the porous structure of SBA-15 type materials. Once the nanofibers were formed, they were functionalized using different thermal and chemical conditions, with the purpose of modifying their surface properties, like texture and surface chemistry; then, their hydrogen uptake capacity was measured and their physico-chemical properties were studied by IR spectroscopy, XPS, Capacitance and TEM. PSDFs were modeled by NLDFT and QSDFT procedures [16]. The surface fractal dimension was obtained by several methods, such as: the Neimark–Kiselev equation [17], Box-counting [18], Information [19] and Perimeter-area [20]. The discussion of results is specially focused to the influence of the functional groups on the hydrogen uptake capacity of carbon nanofibers.

## 2. Experimental

### 2.1. Preparation of UFCNFs and FCNFs materials

#### 2.1.1. Synthesis of SBA-15

Mesoporous silica SBA-15 type materials were prepared using the triblock EO<sub>20</sub>PO<sub>70</sub>EO<sub>20</sub> copolymer (Pluronic 123, Aldrich) and TEOS (Aldrich) as a silica source, as described elsewhere [21]. In a typical synthesis 4 g of triblock polymer was added to 162 ml of 1.5 M hydrochloric acid aqueous solution, then it was stirred at 318 K for 2 h. Next, 9 g of TEOS were added drop-wise and the mixture was stirred at the same temperature for 24 h. The synthesized materials were kept at 363 K for 24 h under static conditions. The final products were filtered, washed with distilled water and dried at 353 K for 24 h. The synthesized samples were calcined under air atmosphere at 823 K.

#### 2.1.2. Synthesis of carbon nanofibers

Carbon nanofibers were prepared using the template method similar to the one reported by Ryoo et al. [22]. For this, SBA-15 was mixed with sucrose solution (C<sub>12</sub>H<sub>22</sub>O<sub>11</sub>, from Aldrich), sulfuric acid (H<sub>2</sub>SO<sub>4</sub>, Merk) and distilled water; once homogenized the mixture was dried at 373 K for 6 h in an inert atmosphere. Afterward, the temperature was increased up to 473 K, then the mixture was dried again for 6 h. A second impregnation was performed by the procedures mentioned above, then after drying under similar conditions the materials were pyrolyzed under inert atmosphere (N<sub>2</sub>, 99%) at 1273 K for 1 h. The molar ratio used for the first impregnation was 1 Sucrose/0.4829H<sub>2</sub>SO<sub>4</sub>/113.805H<sub>2</sub>O; for the second impregnation the molar ratios were the following: 1 Sucrose/0.335H<sub>2</sub>SO<sub>4</sub>/152H<sub>2</sub>O. In order to remove the SBA-15 type siliceous materials, 10% wt HF in aqueous solution was used.

#### 2.1.3. Surface functionalization of carbon nanofibers

Texture and surface chemistry of the UFCNFs materials were modified by oxidation treatments, with the purpose of generating surface functional groups. For this, the carbonaceous materials were exposed to HNO<sub>3</sub> aqueous solutions (Aldrich, reagent grade) under microwave irradiation at 383 K and 393 K (3 min) in a microwave synthesis system (Synthos 3000 from Anton-Paar). The materials obtained were labeled with distilled water, filtered and dried at 353 K overnight.

## 2.2. Characterization

### 2.2.1. Transmission electron microscopy

The FCNFs materials were studied by Transmission Electron Microscopy which was performed using a FEI Tecnai G2 30 transmission electron microscope at 300 keV. Dry samples were prepared on a holey carbon grid.

### 2.2.2. Infrared spectroscopy

The FCNFs and UFCNFs materials were analyzed at room temperature by infrared spectroscopy using a FT-IR Bruker spectrophotometer model Vertex 70. Spectra were recorded after 16 scans at a resolution of 2 cm<sup>-1</sup>. For this propose KBr pellets containing 0.1% carbon nanofibers were used.

### 2.2.3. Adsorption measurements

N<sub>2</sub> sorption isotherms at 76 K of carbon nanofibers were determined using an automatic Quantachrome Autosorb 3B instrument. Prior to the adsorption run, all the samples were outgassed for 12 h at 473 K. N<sub>2</sub> and He gases (UHP grade) were used for the operation of the sorption apparatus. The specific surface areas were calculated from desorption isotherms and the BET equation, and the pore structure parameters were determined by NLDFT and QSDFT procedures.

### 2.2.4. Fractal dimension from TEM micrographs

The fractal dimensions of solid clusters were determined by the box-counting method [23,24] using the commercial BENOIT 1.3 software [25]. The fractal dimensions D<sub>p</sub> and D<sub>f</sub> were determined by perimeter-area and information methods, which were included in the BENOIT software.

### 2.2.5. Hydrogen storage measurements

Hydrogen uptake capacity of carbon nanofibers was evaluated using a Micromeritics ASAP 2020, by the application number 136, as follows:

- Outgassing conditions. First, outgassing was carried out in a preparation port. The carbon nanofibers (substrate) were dried at 283 K min<sup>-1</sup> up to 363 K (5 mmHg s<sup>-1</sup>) then were heated at 283 K min<sup>-1</sup> up to 573 K for 300 min. A second outgassing was carried out by the analysis port under vacuum pressure conditions, by heating at 283 K min<sup>-1</sup> up to 573 K for 21 h.
- Analysis conditions: 10 points were taken initially at 850 mmHg of pressure under isothermal conditions. Liquid nitrogen at 76 K was employed in the bath (this is the boiling temperature of N<sub>2</sub> at Mexico City) and hydrogen 99.998% purity as adsorbate.

### 2.2.6. Electrochemical properties

Electrochemical properties were measured at 298 K using a conventional three-electrode test electrochemical cell with an aqueous solution 0.5 M H<sub>2</sub>SO<sub>4</sub> (Merck) was used as electrolyte and argon gas (99.999%, chromatographic grade) as purgative. A platinum mesh was used as the counter electrode and Hg/Hg<sub>2</sub>SO<sub>4</sub>/

<sup>1</sup> A list of symbols and acronyms utilized in this work is provided just above the References.

0.5 M H<sub>2</sub>SO<sub>4</sub> (MSE = 0.680 V/NHE) as the reference electrode. The experiments were performed in a VersaSTAT 3 (METEK-PAR) potentiostat and a Pine MSRX rotation speed controller. Prior to the electrochemical measurements, the solution was degassed with argon for 10 min. The potentials reported herein are relative to a standard hydrogen electrode (NHE). Prior to obtaining the capacitance measurements, cyclic voltammetry (CV) was performed from 0.0 to 1.2 V at 100 mV s<sup>-1</sup> in an argon-saturated electrolyte which allowed to cleaning the electrode surface and helped elimination of impurities and oxides. Ten cycles were required to stabilize the current-potential signal. An ink-type electrode was employed as a working electrode. For the electrochemical experiments, 8 µl of a sonicated mixture of 1 mg catalyst, 32 µl ethyl alcohol (spectrum grade), and 4 µl of a 5 wt% Nafion® solution (Du Pont, 1000 EW) were deposited onto a glassy carbon electrode (GC) with a cross-sectional area of 0.19 cm<sup>2</sup>.

#### 2.2.7. Surface functional groups

X-ray photoelectron spectra were recorded with a Kratos His spectrometer which was equipped with a dual anode (Mg/Al) and a monochromatic Al source, a 127-mm hemispherical analyzer with a detection system containing 5 channeltrons, and a magnetic immersion lens that was used to provide high sensitivity and charge compensation. The smallest spot size recorded was about 30 µm.

### 3. Results and discussion

#### 3.1. Transmission electron microscopy

TEM photomicrographs of Fig. 1 display information about the textural properties of the carbon nanofibers such as separation between nanofibers and quasi-parallel channels running among nanofibers.

TEM photomicrographs show the different textures achieved by the chemical and thermal conditions. Fig. 1(b–d) correspond to materials treated with HNO<sub>3</sub>:H<sub>2</sub>O solution and submitted to microwave irradiation. The images portray a topology which keeps the typical geometry of a SBA-15 matrix. Particularly, the images 1(c) and 1(d) displayed a morphology, which lets us think in the flexibility as a possible mechanical property of these carbon nanofibers. A model of condensation inside interstitial spaces formed by four carbon nanofibers with a cavity surrounded by four throats is shown in Fig. 2. The access to the main cavity is made through neighboring cavities, which are narrower than the main cavity. The pore-throats are like rectangular chambers which are formed by two fibers, as shown in Fig. 2. Moreover, the topology suggests that the void structure is formed through chambers which are interconnected by narrower necks. Also, a slight separation between nanofibers is be observed in Fig. 1.

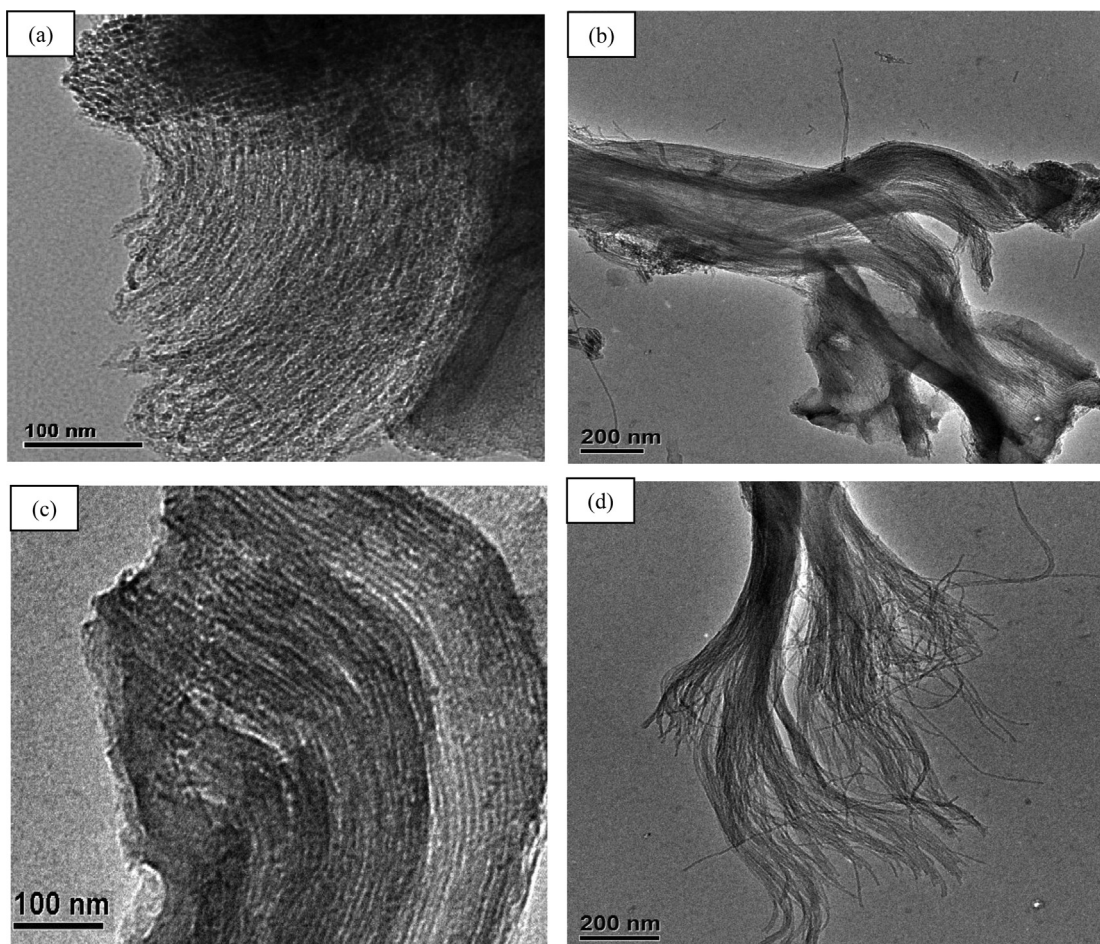


**Fig. 1.** TEM photomicrographs, which portray the carbon nanofibers before and after the functionalization process. (a) UFCNFs, (b) FCNFs-I, (c) FCNFs-II and (d) FCNFs-III. Important changes in the textural properties were achieved by chemical and thermal treatment especially on those FCNFs-IV materials.

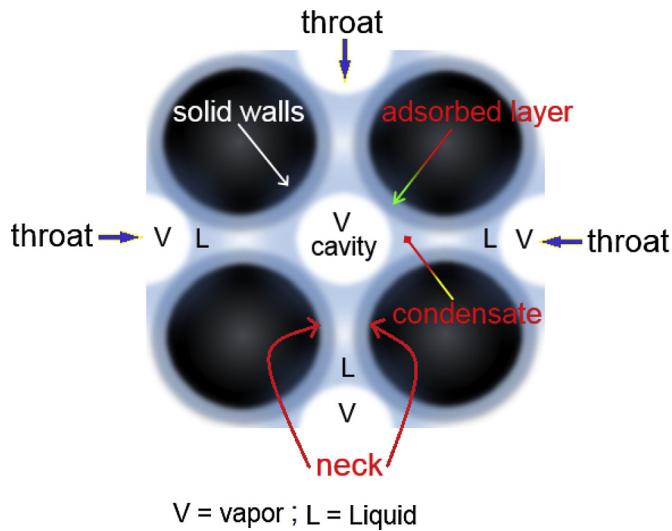


**Fig. 2.** Model of condensation inside interstitial spaces (pore network) formed by four carbon nanofibers. The L–V menisci are formed at necks and these are moved towards the cavity until fill it with condensate.

### 3.2. Infrared spectroscopy

FT-IR spectra of the UFCNFs and FCNFs materials are shown in Fig. 3. FT-IR spectra show the same absorption bands for the carbon samples at  $1724 \pm 45 \text{ cm}^{-1}$ ,  $1595 \pm 45 \text{ cm}^{-1}$  and  $1210 \pm 55 \text{ cm}^{-1}$ . According to the literature [26], the bands localized at  $1700 \pm 45 \text{ cm}^{-1}$ ,  $1595 \pm 45 \text{ cm}^{-1}$  and  $1210 \pm 55 \text{ cm}^{-1}$  arise from C=O stretching vibrations deriving from –COOH groups (carboxylic acids). On the other hand, both FCNFs and UFCNFs materials showed absorbance bands at  $1211$  and  $1583 \text{ cm}^{-1}$ , while the band at  $1724 \text{ cm}^{-1}$  is absent in the UFCNFs materials (see Fig. 3). In addition, this material shows somewhat broadened bands as compared to the bands of the FCNFs materials. These facts must be a consequence of the meager functionalization on their surfaces, which will be assessed by other methods later.

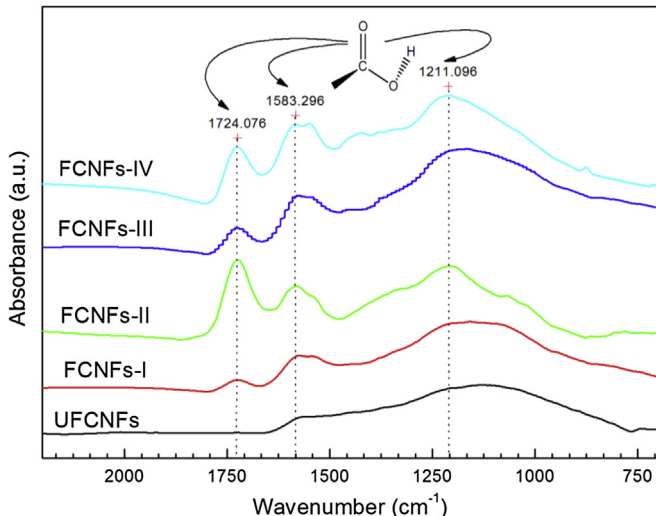


**Fig. 3.** FT-IR spectra which show the presence of –COOH groups chemisorbed on those FCNFs materials. Dashed lines indicate no shift between bands.

### 3.3. Textural properties

#### 3.3.1. $N_2$ adsorption isotherms

$N_2$  isotherms of the FCNFs materials are illustrated in Figs. 4 and 5b–d which display the type H3 hysteresis loops [27]; in comparison, the UFCNFs materials almost match type H4 isotherm [27]. Fig. 5(a) (UFCNFs) shows that the  $N_2$  adsorption is higher than those FCNFs materials. The adsorption percentage for the former materials is significantly larger than those FCNFs materials (more than twice). These latter show a close linearity in  $P/P^\circ \in [0.05–0.88]$  as shown in Fig. 4. This behavior might be attributed to multilayer growth into empty spaces, i.e., cavities and throats. The adsorption isotherm at around  $P/P^\circ \sim 0.88$  suggests the formation of condensate at the neck level (Fig. 2). At  $P/P^\circ > 0.88$ , the liquid–vapor menisci move towards the cavity until this is filled up with condensate. This may explain the large increase of  $N_2$  adsorbed at around  $P/P^\circ \sim 1$  as shown in Fig. 4. In contrast, desorption curve (Fig. 4) shows that emptying of cavities by capillary evaporation might be followed by emptying of throats. Therefore, the sorption isotherms for these materials are consistent with the sorption process model shown in Figs. 1, 2 and 4.

The pore structure parameters of UFCNFs and FCNFs materials are reported in Table 1 where some changes in  $S^{\text{BET}}$ ,  $V_p^{\text{NLDFT}}$  and  $V_{\text{iw}}^{\text{NLDFT}}$  are verified as follows:

- At 383 K, there is an increase of 2%  $V_p^{\text{NLDFT}}$  and an increase of 4% in  $V_{\text{iw}}^{\text{NLDFT}}$  with the increase from 25 to 50 vol.%  $\text{HNO}_3$ .
- At 393 K, there are increases of 30, 40 and 10% in  $S^{\text{BET}}$ ,  $V_p^{\text{NLDFT}}$  and  $V_{\text{iw}}^{\text{NLDFT}}$  respectively with the increase from 25 to 50 vol.%  $\text{HNO}_3$ .

Thus, Table 1 shows that the carbon nanofibers were sensitive to thermal treatments during the functionalization process, and it plays a role in the final textural properties of carbon nanofibers:

- For a concentration of 25 vol.%  $\text{HNO}_3$  a decrease of 16, 23 and 9% occurs for  $S^{\text{BET}}$ ,  $V_p^{\text{NLDFT}}$  and  $V_{\text{iw}}^{\text{NLDFT}}$  with an increase of about 10 K.
- For a concentration of 50 vol.%  $\text{HNO}_3$  a decrease of about 5, 77 and 15% occurs for  $S^{\text{BET}}$ ,  $V_p^{\text{NLDFT}}$  and  $V_{\text{iw}}^{\text{NLDFT}}$  with an increase of about 10 K.

Therefore, the changes pointed out before reveal that  $V_p^{\text{NLDFT}}$  value was the most sensitive to the oxidation treatment.

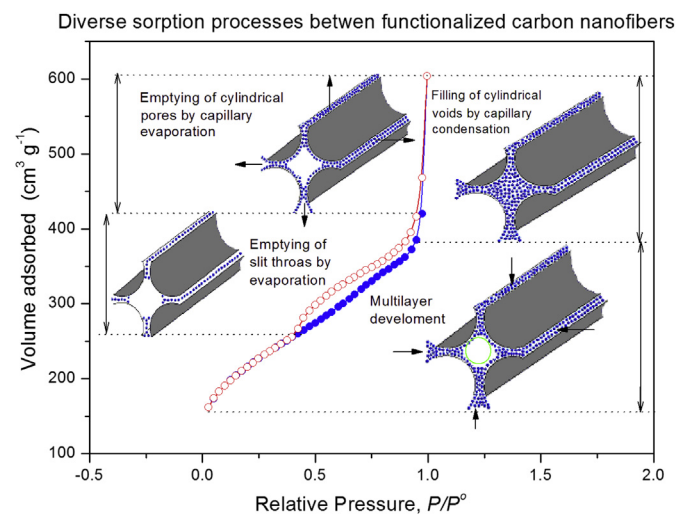


**Fig. 4.** Graphical sequence of the  $N_2$  sorption processes on carbon nanofibers as a function of the relative pressure. The picture corresponds to FCNFs-I materials.

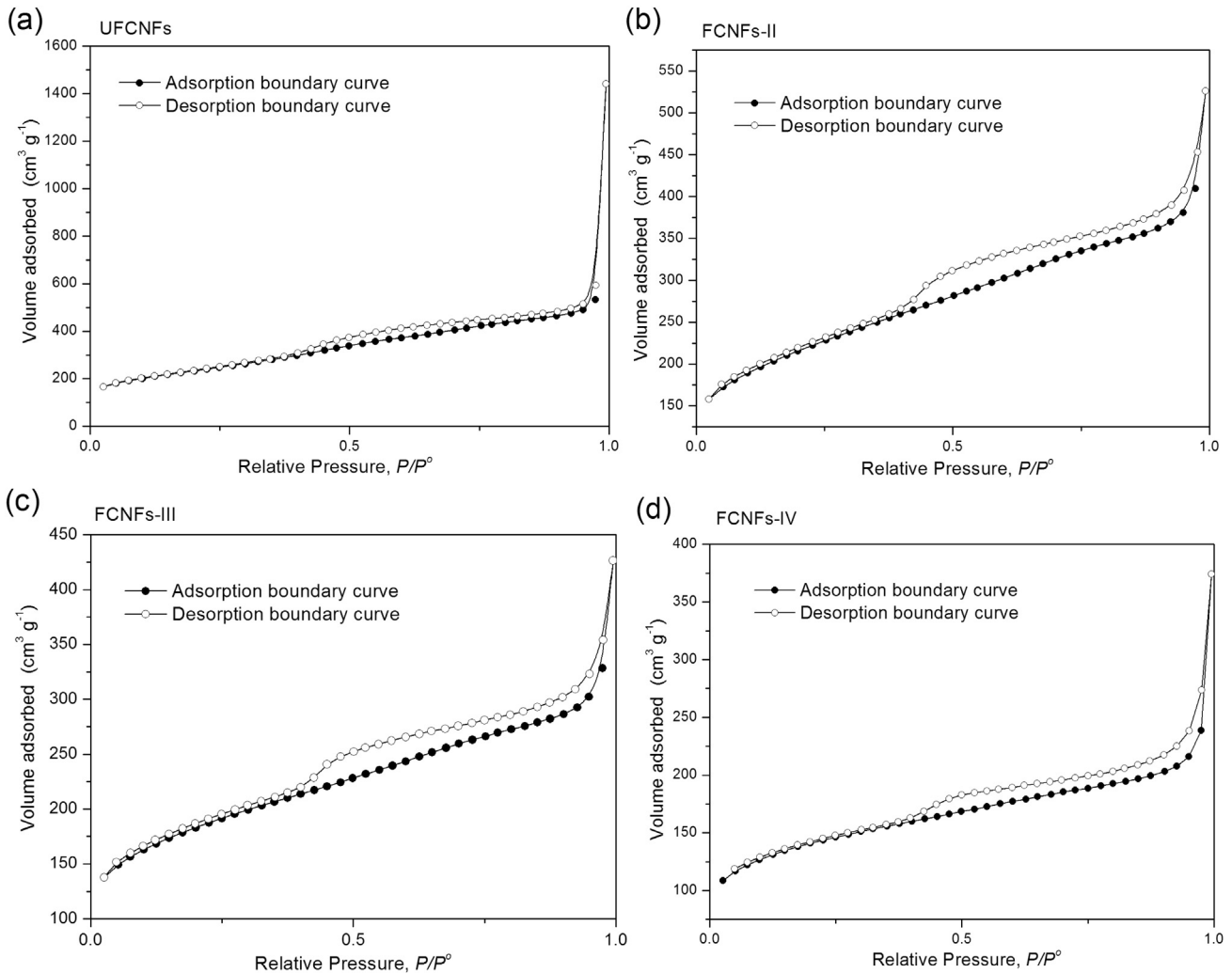


**Fig. 5.**  $\text{N}_2$  sorption isotherms at 76 K on functionalized carbon nanofibers at different thermal and chemical conditions. (a) UFCNFs, (b) FCNFs-II, (c) FCNFs-III and (d) FCNFs-IV.

Regarding the increase of  $V_{\text{iw}}^{\text{NLDFT}}$  values after the functionalization (Table 1), it is thought that microcorrosion on pore walls might occur in parallel with the functionalization process. The surface area and pore volume of the UFCNFs materials are significantly larger than those related to FCNFs materials. Additionally, the surface areas decreased from 775 to  $476 \text{ m}^2 \text{ g}^{-1}$  as the functionalization process went by. A similar effect can be verified for the total pore volume ( $V_p^{\text{NLDFT}}$ ), which decreased from 664 to  $294 \text{ mm}^3 \text{ g}^{-1}$ .

### 3.3.2. Micropore analysis

Figs. 4 and 5 show the region between the two linear portions which represents the transition occurring when the micropores

become filled ( $P/P^\circ \sim 0.05$ ) while the multilayer adsorption continues in the larger pores. The adsorption isotherms show an increase in  $\text{N}_2$  uptake at low relative pressures, from this, one can infer that a relatively small fraction of micropores is present (see Table 1). The UFCNFs materials have a micropore volume of  $144 \text{ mm}^3 \text{ g}^{-1}$  and it diminishes to about  $95 \text{ mm}^3 \text{ g}^{-1}$  after the functionalization process. This could be attributed to diffusion constraints of  $\text{N}_2$  into FCNFs materials, as schematized in Fig. 6.

### 3.3.3. Pore-size distribution

The PSDF curves of UFCNFs and FCNFs materials were obtained by the NLDFT method. It was applied to the desorption branch of the isotherms [28]. The PSDF curves corresponding to FCNFs materials are shown in Fig. 7. For the purpose of comparison, the PSDF-UFCNFs curve was also included in Fig. 7. The mean pore sizes were obtained by the NLDFT method and desorption data (Table 1). Taking into account that the functionalization process has not yet taken place, the PSDF-UFCNFs curve is sharper than those PSDF-FCNFs curves as shown in Fig. 7(a), this can be because the pore structure of the UFCNFs materials is not hindered to adsorption of condensate. So, the PSDF curves of the FCNFs materials are similar to each other (see Fig. 7(b–d)).

**Table 1**  
Surface areas and pore structure parameters of UFCNFs and FCNFs materials.

| Materials | $S^{\text{BET}}$<br>( $\text{m}^2 \text{ g}^{-1}$ ) | $V_p^{\text{NLDFT}}$<br>( $\text{mm}^3 \text{ g}^{-1}$ ) | $D_p^{\text{NLDFT}}$<br>(nm) | $V_{\text{iw}}^{\text{NLDFT}}$<br>( $\text{mm}^3 \text{ g}^{-1}$ ) | $V_{\text{Mi}}$<br>( $\text{mm}^3 \text{ g}^{-1}$ ) |
|-----------|---|--|------------------------------|--|---|
| UFCNFs    | 810   | 664  | 3.5/4.9                      | 120  | 144   |
| FCNFs-I   | 716   | 507  | 2.3/2.6/3.5/4.9              | 164  | 101   |
| FCNFs-II  | 727   | 522  | 1.9/2.6/3.5/4.9              | 157  | 82  |
| FCNFs-III | 600   | 412  | 1.9/2.3/2.6/3.5/4.9          | 150  | 98  |
| FCNFs-IV  | 451   | 294  | 1.96/2.3/2.6/3.5/4.9         | 136  | 95  |

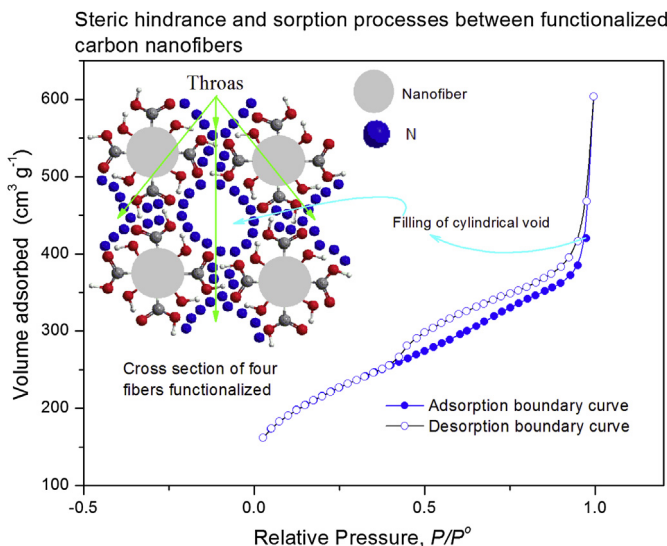


**Fig. 6.** Theoretical picture of steric hindrance of the adsorption-desorption nitrogen on carbon nanofibers after the functionalization process. The  $-COOH$  groups chemisorbed on carbon nanofibers are illustrated at the left hand side of the figure.

### 3.3.4. Fractal analysis

**Fig. 8** displays the surface fractal analysis through the Neimark–Kiselev method for FCNFs and UFCNFs materials. An increase of 10 K in the thermal treatment between FCNFs-I and FCNFs-III,  $D_{S(Desorption)}$  increases from 2.80 to 2.84. In the case of FCNFs-II and FCNFs-IV materials,  $D_{S(Desorption)}$  increases from 2.81 to 2.94.

In regard to an increase from 25 to 50% vol.  $HNO_3$ : between FCNFs-I and FCNFs-II,  $D_{S(Desorption)}$  increases from 2.80 to 2.81 and between FCNFs-III and FCNFs-IV,  $D_{S(Desorption)}$  increases from 2.84 to 2.94. Also, noteworthy that UFCNFs have the lowest  $D_{S(Desorption)}$  value, which might be related to the steric hindrance produced by functional groups on the surface, as it was pointed out before.

Fractal dimension values higher imply geometric surface patterns more complex. Thereby, the different thermal and chemical conditions used in this work have conferred different textural properties to those carbon nanofibers.

On the other hand, considering the Kelvin equation (1) and **Fig. 8(b)**, we can note that the fractality is held for  $r_k$  values smaller than 1.041 nm for the FCNFs-II materials while for FCNFs-III and UFCNFs materials the fractality is held for  $r_k$  values smaller than 1.333 and 1.08 nm respectively; additionally, the  $D_s$  values fall in a region where the mean pore diameter is smaller than the mean pore size, which means that those  $D_s$  values describe the finer surface details within pores.

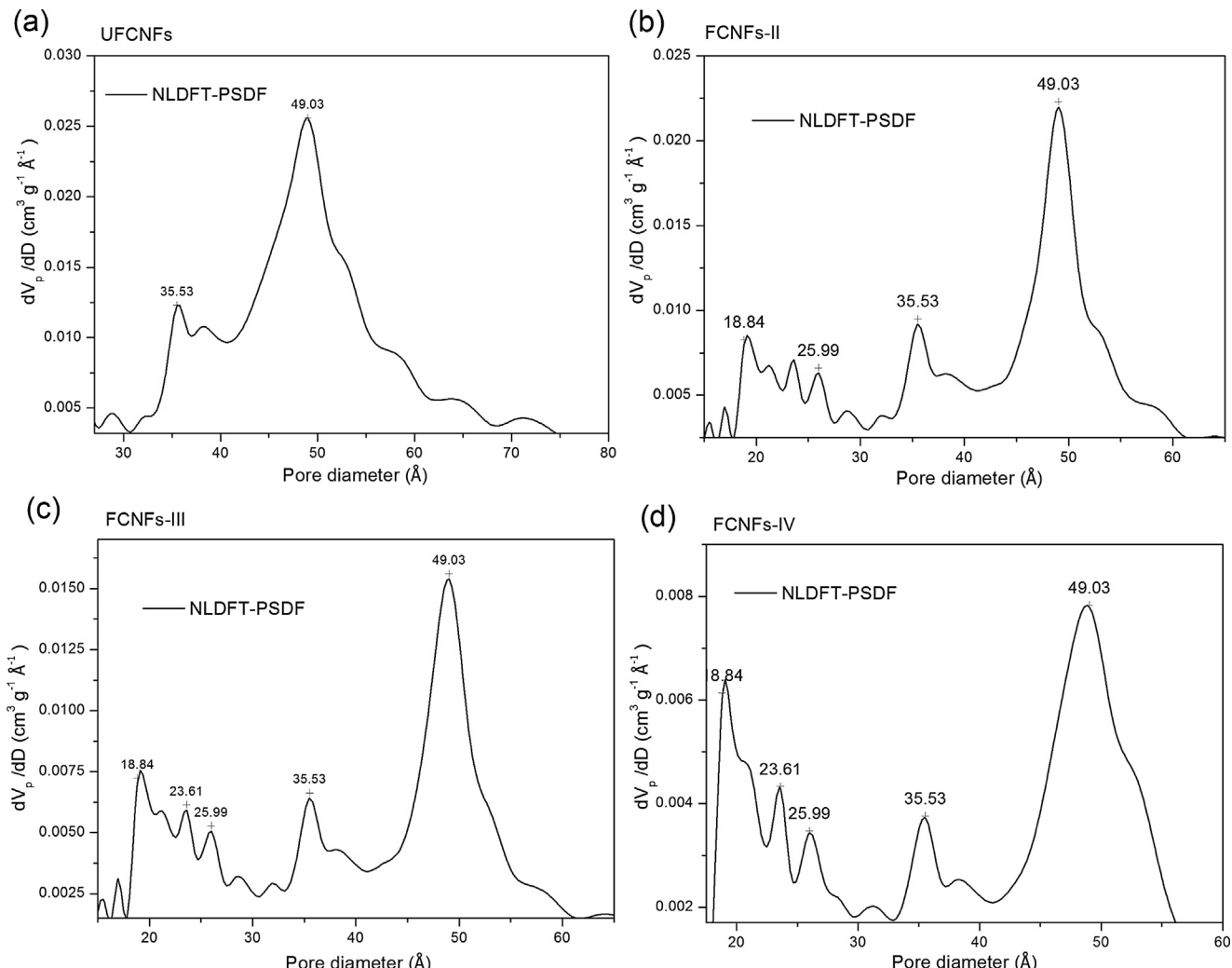


**Fig. 7.** NLDFT-PSDF curves of carbon nanofibers, which are functionalized at different thermal and chemical conditions. (a) UFCNFs, (b) FCNFs-II, (c) FCNFs-III and (d) FCNFs-IV.

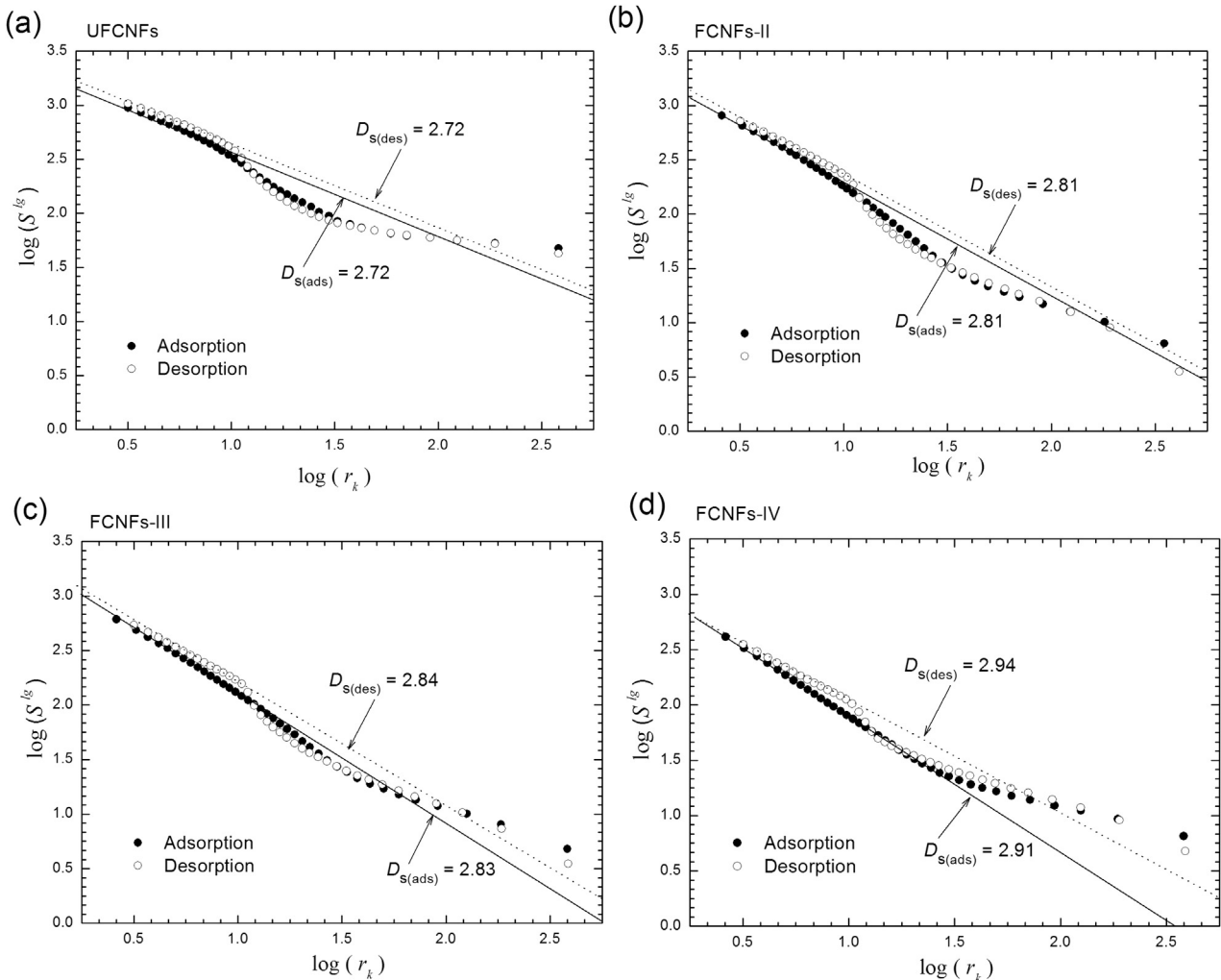


**Fig. 8.** Neimark–Kiselev fractal analysis of the adsorption–desorption isotherms of carbon nanofibers. (a) UFCNFs, (b) FCNFs-II, (c) FCNFs-III and (d) FCNFs-IV.

The Kelvin equation [29]:

$$r_k = \frac{2\gamma V_m}{RT \ln\left(\frac{P^0}{P}\right)} \quad (1)$$

being  $r_k$  the radius of curvature of adsorbate–vapor interface;  $R$  the universal gas constant;  $T$  the adsorption temperature;  $\gamma$  the  $l \leftrightarrow g$  interfacial surface tension;  $V_m$  the adsorbate molar volume and  $P^0/P$  the relative pressure (where  $P^0$  is the saturation pressure).

Additionally, by comparing FT-IR spectra (Fig. 3) with Table 2, we might suggest that the chambers formed among carbon nanofibers are hindered by the carboxylic groups chemisorbed as shown in Figs. 3 and 6. Thereby, the topology of the FCNFs materials depends of the functionalization degree; accordingly, the fractal nature of the FCNFs materials depends of thermal and chemical treatments.

### 3.3.5. Fractal dimension through TEM photomicrographs

Perimeter-Area, Box-counting and Information procedures were used on TEM photomicrographs to determine the fractal dimension of UNFNFs and FCNFs materials (Table 2). The calculations covered the interval between 100 and 200 nm. The  $D_R$ ,  $D_B$  and  $D_I$  values were obtained from the plots shown in Fig. 9, which reflect mainly the segregation degree on these nanofibers rather than the fine

molecular aspects (Fig. 1). Three additional commentaries can help to clarify differences within TEM photomicrographs (Fig. 1 and Table 2).

- Box-counting results ( $D_B$ ) reveal an increase in the complexity of the topology (from 1.57 to 1.83) on these materials. Perhaps, fiber separation took place during chemical and thermal treatments (Fig. 10).

**Table 2**  
Fractal dimension data using different methods on UFCNFs and FCNFs materials.

| Method of analysis                             | UFCNFs          | Materials       |                 |                 |                 |
|--|-----------------|-----------------|-----------------|-----------------|-----------------|
|  |                 | FCNFs-I         | FCNFs-II        | FCNFs-III       | FCNFs-IV        |
| Neimark–Kiselev ( $D_{S(\text{Adsorption})}$ ) | 2.72            | 2.43            | 2.81            | 2.83            | 2.91            |
| Neimark–Kiselev ( $D_{S(\text{Desorption})}$ ) | 2.72            | 2.80            | 2.81            | 2.84            | 2.94            |
| Box-counting ( $D_B$ )                         | $1.77 \pm 0.01$ | $1.57 \pm 0.08$ | $1.80 \pm 0.02$ | $1.81 \pm 0.02$ | $1.83 \pm 0.01$ |
| Information ( $D_I$ )                          | $1.81 \pm 0.01$ | $1.63 \pm 0.01$ | $1.76 \pm 0.01$ | $1.80 \pm 0.06$ | $1.86 \pm 0.01$ |
| Perimeter-area ( $D_P$ )                       | $1.28 \pm 0.04$ | $1.56 \pm 0.06$ | $1.35 \pm 0.08$ | $1.35 \pm 0.31$ | $1.34 \pm 0.02$ |

$D_S$  scaling interval  $\in [2,3]$ ;  $D_B$ ,  $D_I$  and  $D_P$  are measured from TEM microphotographs;  $D_B$  scaling interval  $\in [1,2]$ ;  $D_I$  scaling interval  $\in [1,2]$ ;  $D_P$  scaling interval  $\in [1,2]$ .

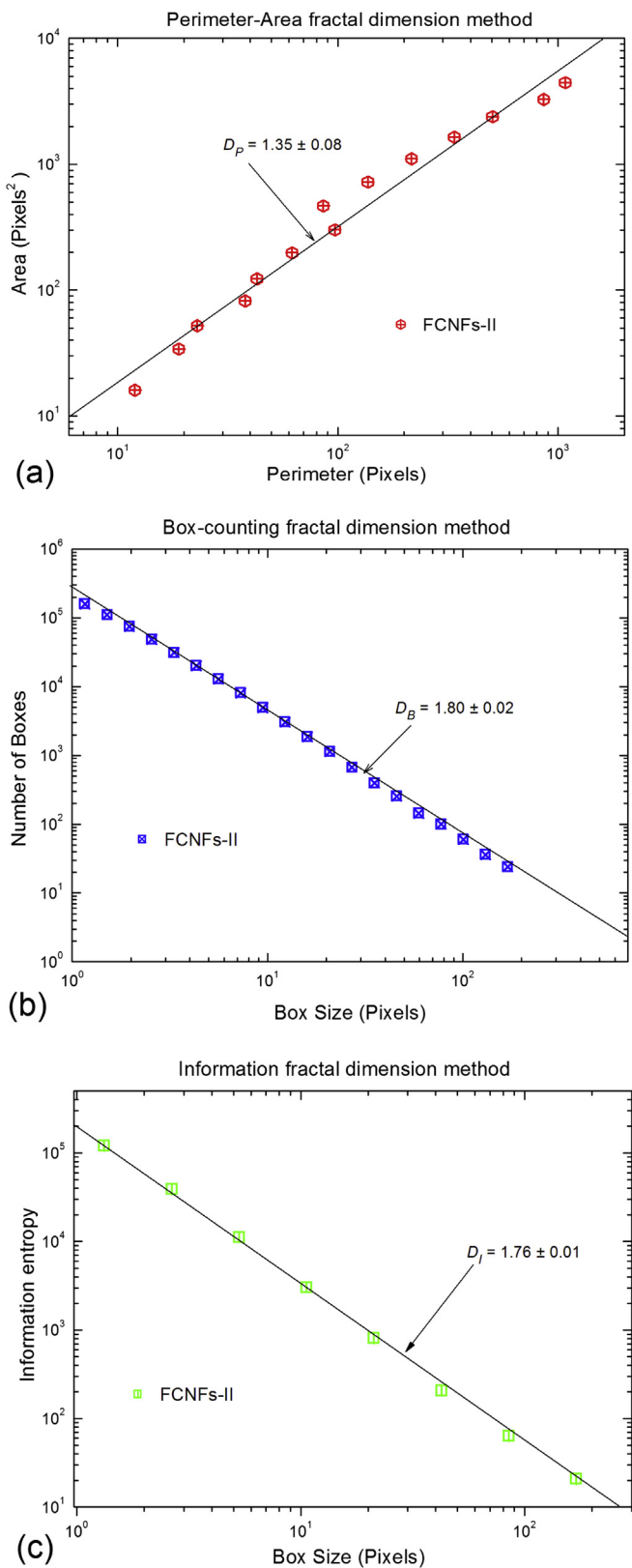


**Fig. 9.** Representative Benoit runs performed on FCNFs TEM photomicrograph. (a) Perimeter-area, (b) Box-counting and (c) Information methods.

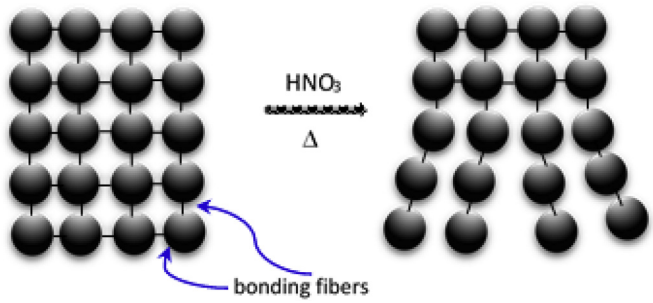


**Fig. 10.** Schematic representation (cross-section) of a bunch of carbon nanofibers before and after the chemical treatment with a HNO<sub>3</sub> solution. The carbon fibers much thinner (bonding fibers) are removed by the thermal and chemical treatments.

- The same behavior can be observed for the  $D_I$  values, from 1.63 to 1.86 (see Table 2).
- Regarding Perimeter-area results, the  $D_p$  value of the FCNFs-I materials is higher (1.56) than the other materials (1.34), what means that the nanofibers corresponding to type II, III and IV were smoothed somehow.

### 3.4. Hydrogen storage

The hydrogen storage capacity of the UFCNFs materials (Fig. 11) as a function of  $P/P^\circ$  displays a type I isotherm, which is typical for those cases when the adsorption is limited to only a few molecular layers on materials. This adsorption isotherm is typical of microporous materials, where the asymptotic approach to a limiting quantity indicates that all the cavities are occupied [29]. One observes that at relative low pressures the higher uptake (about 1.4 wt %) is governed by the accessible micropore volume rather than by internal surface area. With regard to hydrogen uptake capacity of the FCNFs materials, the main differences from each other are displayed in Fig. 12.

It should be noted that due to technical limitations of ASAP-2020 equipment, it is not possible to know the maximum hydrogen uptake of each material, i.e., for pressures higher than 1 atm.

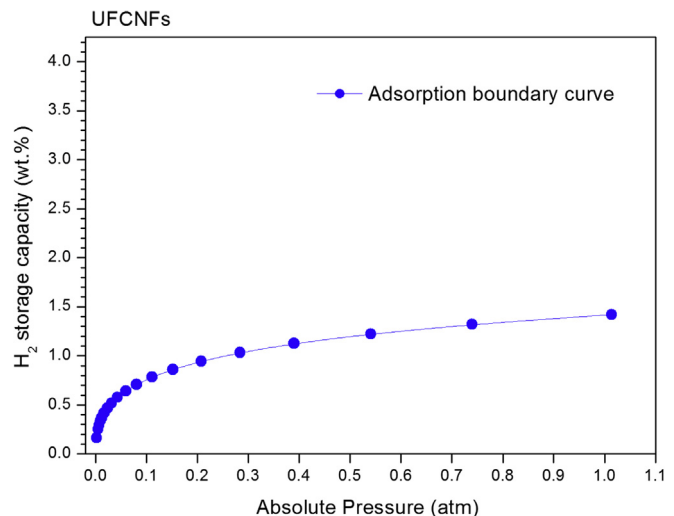


**Fig. 11.** Hydrogen adsorption curve as a function of the relative pressure for unfunctionalized carbon nanofibers (UFCNFs).

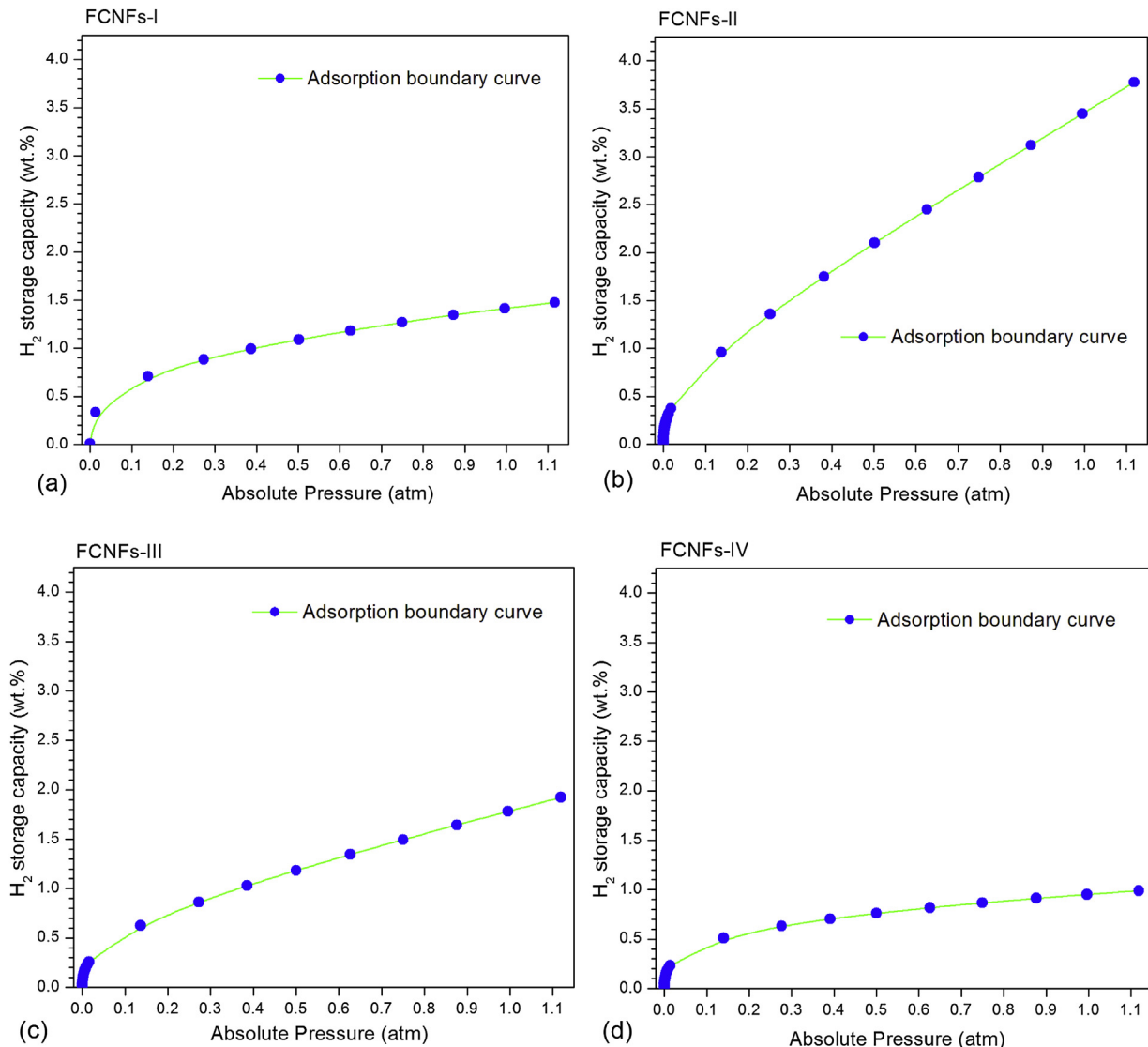


**Fig. 12.** Hydrogen adsorption curve as a function of the relative pressure for different functionalized carbon nanofibers. (a) FCNFs-I, (b) FCNFs-II, (c) FCNFs-III and (d) FCNFs-IV.

The first thing to note in Fig. 12 is the hydrogen uptake that each type of carbon nanofibers can achieve at 1.1 atm. These adsorptions are ordered as follows:

$$\approx 3.8\text{wt.\%} > \approx 1.8\text{wt.\%} > \approx 1.4\text{wt.\%} > \approx 1.0\text{wt.\%}$$

FCNFs – II > FCNFs – III > FCNFs – I > FCNFs – IV

Taking into account all values reported in Table 3 (except those for FCNFs-IV materials), one can note that the values highest correspond to those FCNFs-II materials.

**Table 3**

$H_2$  storage capacity achieved by FCNFs materials at  $P = 1.1$  atm, capacitance data, carboxylic acids concentration and BET surface areas.

| Material  | $S^{\text{BET}}$<br>( $\text{m}^2 \text{g}^{-1}$ ) | [–COOH]<br>(%) | C<br>( $\text{mF cm}^{-2}$ ) | $H_2$ storage capacity<br>(wt%) |
|-----------|--|----------------|------------------------------|---------------------------------|
| FCNFs-I   | 716  | 3.47           | 143.17                       | 1.4                             |
| FCNFs-II  | 727  | 3.96           | 173.76                       | 3.8                             |
| FCNFs-III | 600  | 3.63           | 50.46                        | 1.8                             |
| FCNFs-IV  | 451  | 6.63           | 41.16                        | 1.0                             |

The [–COOH] values were obtained by XPS and show a difference of 0.16% between FCNFs-I and FCNFs-III materials, what may be compensated by the difference between their surface areas. On the other hand, although [–COOH] and C values of FCNFs-I are lower than those FCNFs-II materials, their  $S^{\text{BET}}$  values are very close to each other, what implies that the C value of FCNFs-II materials depends of the amount of –COOH groups on the FCNFs-II surface. A high [–COOH] on the FCNFs surface allows to achieve a better continuous layer of negative charge on surface and thus a high C value, since the C value depends of the charge of the double layer. With respect to FCNFs-IV materials, their [–COOH] value is the highest among FCNFs materials, but their  $S^{\text{BET}}$  value is the lowest; accordingly, their C value too.

Taking into account the results discussed above, it appears that  $H_2$  storage capacity of the FCNFs materials depends on the functionalization degree and the distribution of the –COOH groups on the surface.

Another important change made by the functionalization process into textural properties of the carbon nanofibers can be seen in Fig. 1. TEM photomicrograph (d) shows spaces among nanofibers bigger than those shown in Fig. 1(c). Considering Table 3, one might

suggest that the space among nanofibers too wide, or too narrow leads to FCNFs with less hydrogen uptake capacity (see Figs. 1d, 2 and 10 and 12).

A first explanation might be that the spaces pointed out before arise from the repulsion between surface groups, and a second: carbon fibers much thinner (which play a role as bonding fibers to keep together these carbon nanofibers) are removed by the chemical treatment (see Figs. 1d and 10).

Looking for other results to supplement or reinforce the results mentioned above, Quenched Solid Density Functional Theory (QSDFT) and the nitrogen sorption data were employed. In QSDFT the solid is modeled using the distribution of solid atoms rather than the source of the external potential field. The QSDFT method takes into account the effects of surface roughness and heterogeneity explicitly; moreover, it eliminates artificial gaps in the pore size distributions, what leads to results more accurate. QSDFT-PSDF curves were obtained for the FCNFs materials and they are plotted in Fig. 13.

In all materials, the QSDFT-PSDF-desorption curves at 5.0 nm are higher than those QSDFT-PSDF-adsorption curves. This fact is due to two phenomena:

1) Advanced adsorption [30], i.e., some pores with diameters smaller than that of throats and cavities that just fill with liquid at the point of desorption (see areas B) are filled with condensate and later emptied of it during the first steps of the descending process (cavities having sizes smaller than about 2.6 nm in the case of FCNFs-II materials). Cavities corresponding to areas B are not being filled with condensate along the boundary adsorption path, i.e., for N<sub>2</sub> uptake process those cavities are hindered somehow (for instance, by –COOH groups), and then N<sub>2</sub> molecules are not adsorbed into cavities  $\leq 2.6$  nm. This possibility is taken into account because the kinetic diameter of N<sub>2</sub> is, in fact, larger (20%) than the H<sub>2</sub> diameter (0.36 nm versus 0.28 nm) [31]; however, for H<sub>2</sub> molecules, it is perhaps easier to get into those cavities. In addition, area B corresponding to the biggest advanced adsorption corresponds to FCNFs-II materials. So this phenomenon could contribute to the reason why the highest H<sub>2</sub> uptake.

In each FCNFs material, remarkable differences between the PSDF-adsorption curve and the PSDF-desorption curve are

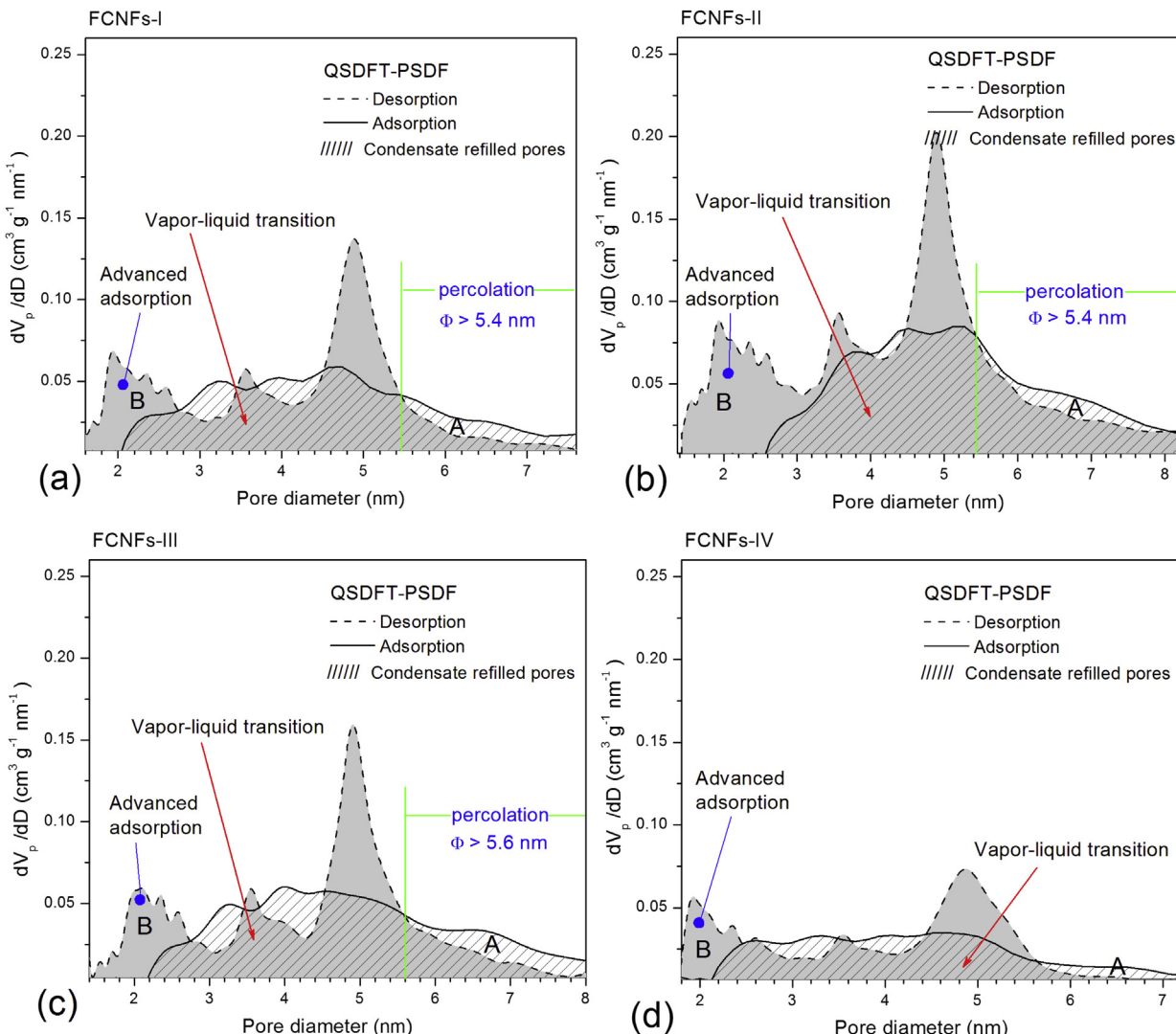


**Fig. 13.** QSDFT-PSDF curves for different carbon nanofibers. (a) UFCNFs, (b) FCNFs-II, (c) FCNFs-III and (d) FCNFs-IV. Lower and upper curves correspond to pore volume derivative of adsorption and desorption respectively. A and B areas correspond to percolation and advanced adsorption phenomena. The zone delimited by the pattern-sparse area over the gray area is the transition between vapor and liquid.

observed. If the pores were not hindered somehow, both PSDF-adsorption and PSDF-desorption would coincide into a unique PSDF line; the reason why the two curves diverge is due to the incidence of both advanced adsorption and pore-blocking [32]. This latter is a consequence of the proximity in sizes between cavities and throats, and perhaps by –COOH groups.

- 2) Some vapor percolation arise at some point along desorption branch (see area A in Fig. 13(b)). This phenomenon reflects that this pore structure is suffering a relative slight pore-blocking in cavities having sizes larger than 5.4 nm.

The areas under the QSDFT-PSDF-adsorption curve display the following order:

$$\left(\frac{dV_p}{dD}\right)^{\text{FCNFs-II}} > \left(\frac{dV_p}{dD}\right)^{\text{FCNFs-III}} > \left(\frac{dV_p}{dD}\right)^{\text{FCNFs-I}} > \left(\frac{dV_p}{dD}\right)^{\text{FCNFs-IV}}$$

which is also consistent with the plots of the H<sub>2</sub> uptake shown in Fig. 12. Although all materials have the same pore diameters (see Fig. 13), the FCNFs-II materials can adsorb more H<sub>2</sub> than other materials. This might attributed to: 1) the total volume pore is higher than other FCNFs materials (see Table 1) and/or 2) a large amount of –COOH groups on their surface. This latter is very important because the electric quadrupole moment of the N<sub>2</sub> molecule,  $\Theta_e$  is  $\approx 0.0$  C m<sup>2</sup> [33], while for the H<sub>2</sub> molecule,  $\Theta_e = 0.5$  C m<sup>2</sup> [34], what means that the charge is not spherically distributed on H<sub>2</sub> molecules, and hence the hydrogen uptake could be more favored by the interactions between –COOH groups and H<sub>2</sub> molecules, thus reinforcing the reason why FCNFs-II materials with C highest are materials having the highest H<sub>2</sub> uptake.

Another thing to note, it is the difference between the PSDFs (shapes) from one to another material. This might be attributed to different geometric patterns or topologies on FCNFs surfaces achieved by the functionalization process, already mentioned before.

#### 4. Conclusions

FCNFs are materials with a high interfacial porosity might be suitable for hydrogen storage. The different preparations used in this work led to different degrees of functionalization, which give rise to different geometric patterns and topologies into the pore network; those arrays can be differentiated from each other by the surface fractal dimension. Functionalization degree and  $\Theta_e$  of H<sub>2</sub> together seems to play a role on hydrogen storage capacity into FCNFs materials. A relationship between the hydrogen storage capacity and the functionalization degree was evidenced. The highest hydrogen uptake corresponds to the carbonaceous materials prepared with 50 vol.% HNO<sub>3</sub> and 383 K (FCNFs-II), as compared to the other materials. This result correlates with the capacitance and final textural properties of those materials. On the other hand, the N<sub>2</sub> uptake decreases with the functionalization degree, which is probably due to the sterical hindrance caused by functional groups chemisorbed into the pore network and  $\Theta_e$  of N<sub>2</sub>; thus, N<sub>2</sub> adsorption depends inversely on the functionalization degree and on the surface fractal dimension, while hydrogen uptake increases with the spacing between the FCNFs, that is, with the repulsion between surface groups.

#### Acknowledgment

F. Galindo-Hernández thanks the financial support from IMP for his postdoctoral research in the Molecular Engineering Coordination.

#### List of symbols and acronyms

|  |   |
|--|---|
| C  | capacitance   |
| -COOH  | carboxylic acids  |
| [–COOH]  | percentage concentration  |
| $dV_p/dD$  | pore volume derivative  |
| $D_S(\text{Adsorption}), D_S(\text{Desorption})$ | fractal dimension obtained by Neimark–Kiselev method  |
| $D_B$  | fractal dimension obtained by Box-counting method   |
| $D_I$  | fractal dimension obtained by Information method  |
| $D_p$  | fractal dimension obtained by Perimeter-area method   |
| $D_p^{\text{NLDFT}}$                             | mean NLDFT pore diameter  |
| FCNFs-I  | functionalized carbon nanofibers type I (functionalized with 25 vol.% HNO <sub>3</sub> and 383 K)   |
| FCNFs-II   | functionalized carbon nanofibers type II (functionalized with 50 vol.% HNO <sub>3</sub> and 383 K)  |
| FCNFs-III  | functionalized carbon nanofibers type III (functionalized with 25 vol.% HNO <sub>3</sub> and 393 K) |
| FCNFs-IV   | functionalized carbon nanofibers type IV (functionalized with 50 vol.% HNO <sub>3</sub> and 393 K)  |
| $\phi$   | cavity diameter   |
| IR   | infrared spectroscopy   |
| NLDFT  | non-local density functional theory   |
| PSDF   | pore size distribution function   |
| QSDFT  | quenched solid density functional theory  |
| $r_k$  | radius of curvature   |
| SBA-15   | mesoporous silica substrate made by a hexagonal array of cylindrical pores                          |
| $S^{\text{BET}}$                                 | BET surface area  |
| TEOS   | tetraethyl-orthosilicate  |
| TEM  | transmission electron microscopy  |
| UFCNFs   | unfunctionalized carbon nanofibers  |
| $V_{\text{IW}}^{\text{NLDFT}}$                   | intrawall pore volume by NLDFT method   |
| $V_{\text{Mi}}$                                  | micropore volume  |
| $V_p^{\text{NLDFT}}$                             | total pore volume by NLDFT method   |
| XPS  | X-ray photoelectron spectroscopy  |
| XRD  | X-ray diffraction   |

#### References

- [1] A. Sigal, M. Villareal, M.I. Rojas, E.P.M. Leiva, Int. J. Hydrogen Energy 39 (2014) 5899–5905.
- [2] S. Yadav, Z. Zhu, C. Ver-Singh, Int. J. Hydrogen Energy 39 (2014) 4981–4995.
- [3] R. Lavanya, V.J. Surya, I. Lakshmi, K. Iyakutti, V. Vasu, H. Mizuseki, Y. Kawazoe, Int. J. Hydrogen Energy 39 (2014) 4973–4980.
- [4] H.P. Veluswamy, R. Kumar, P. Linga, Appl. Energy 122 (2014) 112–132.
- [5] Y. Yanmin, Z. Naiqin, S. Chunsheng, H. Chunnian, L. Enzuo, L. Jiajun, Int. J. Hydrogen Energy 37 (2012) 5762–5768.
- [6] J. Jinhua, G. Qiuning, Z. Zhoujun, X. Kaisheng, H. Juan, Int. J. Hydrogen Energy 35 (2010) 210–216.
- [7] Z. Xiangyu, M. Liquan, Int. J. Hydrogen Energy 34 (2009) 4788–4796.
- [8] R. Ströbel, J. Garche, P.T. Moseley, L. Jörissen, G. Wolf, J. Power Sources 159 (2006) 781–801.
- [9] S. Li, W. Pan, Z. Mao, Int. J. Hydrogen Energy 30 (2005) 643–648.
- [10] A.D. Lueking, L. Pan, D.L. Narayanan, C.E.B. Clifford, J. Phys. Chem. B 109 (2005) 12710–12717.
- [11] D.J. Durbin, C. Malardier-Jugroot, Int. J. Hydrogen Energy 38 (2013) 14595–14617.
- [12] K. Jurewicz, Int. J. Hydrogen Energy 34 (2009) 9431–9435.
- [13] P.S. Fernández, E.B. Castro, S.G. Real, M.E. Martins, Int. J. Hydrogen Energy 34 (2009) 8115–8126.
- [14] M. Jordá-Beneyto, F. Suárez-García, D. Lozano-Castelló, D. Cazorla-Amorós, A. Linares-Solano, Carbon 45 (2007) 293–303.
- [15] E. Terrés, B. Panella, T. Hayashi, Y.A. Kim, M. Endo, J.M. Dominguez, M. Hirscher, H. Terrones, M. Terrones, Chem. Phys. Lett. 403 (2005) 363–366.
- [16] (a) P.I. Ravikovich, A.V. Neimark, Langmuir 18 (2002) 1550–1560;  
 (b) A.V. Neimark, P.I. Ravikovich, A. Vishnyakov, J. Phys. Condens. Matter 15 (2003) 347–365;  
 (c) A.V. Neimark, P.I. Ravikovich, Y. Lin, M. Thommes, Carbon 47 (2009) 1617–1628.
- [17] A.V. Neimark, in: C.A.C. Sequeria, M.J. Hudson (Eds.), *Multifunctional Mesoporous Inorganic Solids*, Kluwer Academic Publishers, Netherlands, 1993.

- [18] Z.L. Jing, D.Z. Lu, H.Y. Guang, *Biophys. J.* 85 (2003) 4041–4046.
- [19] G.L. Baker, J.B. Gollub, *Chaotic Dynamics: an Introduction*, second ed., Cambridge University Press, Cambridge, England, 1996.
- [20] D. Shi, J. Jiang, E. Tian, C. Lung, *J. Mater. Sci. Technol.* 13 (1997) 416–420.
- [21] D. Zhao, J. Sun, Q. Li, G.D. Stucky, *Chem. Mater.* 12 (2000) 275–279.
- [22] S. Jun, S.H. Joo, R. Ryoo, M. Kruk, M. Jaroniec, Z. Liu, *J. Am. Chem. Soc.* 122 (2000) 10712–10715.
- [23] K. Falconer, *Techniques in Fractal Geometry*, Wiley, New York, 1997.
- [24] B.B. Mandelbrot, *The Fractal Geometry of Nature*, Freeman, New York, 1983.
- [25] BENOIT 1.3 <http://www.trusoft-international.com/benoit.html>.
- [26] R.M. Silverstein, F.X. Webster, D. Kiemle, *Spectrometric Identification of Organic Compounds*, seventh ed., John Wiley & Sons, Inc., New York, 2005.
- [27] K.S.W. Sing, D.H. Everett, R.A.W. Haul, L. Moscou, R. Pierotti, J. Rouquerol, T. Siemieniewska, *Pure Appl. Chem.* 57 (1985) 603–619.
- [28] P.I. Rakovitch, A.V. Neimark, *J. Phys. Chem. B* 105 (2001) 6817–6823.
- [29] S. Lowell, J.E. Shields, M.A. Thomas, M. Thommes, *Characterization of Porous Solids and Powders: Surface Area, Pore Size and Density*, first ed., Kluwer Academic Publishers, Netherlands, 2004.
- [30] D.H. Everett, *J. Colloid Interf. Sci.* 52 (1975) 189–198.
- [31] D.W. Beck, *Zeolite Molecular Sieves*, Wiley & Sons, New York, 1974.
- [32] D.H. Everett, in: E.A. Flood (Ed.), *The Solid–Gas Interface*, vol. 2, Dekker, New York, 1967.
- [33] A. Halkier, S. Coriani, P. Jørgensen, *Chem. Phys. Lett.* 294 (1998) 292–296.
- [34] R.F. Borkman, *Chem. Phys. Lett.* 9 (1971) 624–626.